Site mixing induced ferrimagnetism and anomalous transport properties of the Weyl semimetal candidate MnSb$_2$Te$_4$

D. Y. Yan,[1,3] M. Yang,[1,3] P. B. Song,[1,3] Y. T. Song,[1] C. X. Wang,[1,3] C. J. Yi,[1,*] and Y. G. Shi[1,2,3,4]

[1]*Beijing National Laboratory for Condensed Matter Physics and Institute of Physics, Chinese Academy of Sciences, Beijing 100190, China*
[2]*Center of Materials Science and Optoelectronics Engineering, University of Chinese Academy of Sciences, Beijing 100049, China*
[3]*School of Physical Sciences, University of Chinese Academy of Sciences, Beijing 100190, China*
[4]*Songshan Lake Materials Laboratory, Dongguan, Guangdong 523808, China*

MnSb$_2$Te$_4$ has been proposed to have magnetic topological states as a potential Weyl semimetal. We synthesized single crystals of MnSb$_2$Te$_4$ and systematically investigated their structural and physical properties. MnSb$_2$Te$_4$ has an isostructural septuple-layered structure that is similar to the magnetic topological insulator MnBi$_2$Te$_4$ but possesses transpositional Mn and Sb atoms between the sublayers. Magnetic and specific-heat measurements revealed a ferrimagnetic phase transition with a Curie temperature T_C of $\sim$31 K in MnSb$_2$Te$_4$, which originates from the interaction of the interexchanged Mn^{2+} ions. As the temperature decreases below T_C, negative longitudinal magnetoresistance and anomalous Hall effect are observed, implying a non-negligible connection between the magnetism and expected transport carriers that may be driven by topological bands. Our results indicate that ferrimagnetic MnSb$_2$Te$_4$ provides insights for further studies on magnetic topological materials.

I. INTRODUCTION

Time-reversal invariant topological insulators (TIs) have gapless topological boundary states with Dirac conelike dispersions, which are protected by time-reversal symmetry (TRS) [1–4]. TRS plays an important role in the topological quantum states of matter. Introducing magnetism into TIs will gap the topological surface states and produce various exotic topological phenomena such as the topological magnetoelectric effect, axion insulator, and quantum anomalous Hall effect (AHE) [5–14]. Cr-doped (Bi, Sb)$_2$Te$_3$ thin films have been experimentally confirmed to exhibit the QAH effect [12,15,16]. However, the effect usually appears at extremely low temperatures ($<$100 mK) because most magnetic impurities induce strong inhomogeneity in magnetically doped TIs, which hinders further exploration of topological quantum effects.

Intrinsic magnetic topological insulators (MTIs) are ideal materials for studying emergent quantum phenomena at elevated temperatures [17,18] owing to their topologically nontrivial properties and spontaneous magnetic order. Some magnetic topological states have been theoretically proposed [19], such as antiferromagnetic topological insulators (AFMTIs) [17], dynamical axion fields [7], magnetic Dirac semimetals [20–23], and Weyl semimetals [24–26]. Recently, septuple-layered MnBi$_2$Te$_4$ and MnSb$_2$Te$_4$ were found to be intrinsic MTIs. MnBi$_2$Te$_4$ was proposed and experimentally

confirmed to be an intrinsic AFMTI [27–31], and the QHA effect was also observed in MnBi$_2$Te$_4$ thin flakes [32,33]. The evolution of the physical properties of MnBi$_{2-x}$Sb$_x$Te$_4$ was reported by Yan *et al.* [34]. The magnetic structure of polycrystalline MnSb$_2$Te$_4$, measured by neutron scattering, confirmed the presence of interexchange of Mn and Sb atoms, leading to a ferrimagnetic ground state [35]. MnSb$_2$Te$_4$ is proposed to be an ideal system for testing the theory of electron-electron interaction correction to the AHE [36]. Theoretical calculations also propose that ferromagnetic and site-mixing ferrimagnetic MnSb$_2$Te$_4$ can be tuned to be the simplest type-I and type-II Weyl semimetals, respectively [37]. The growth of single crystals is urgently required for further analyses of the topological state in MnSb$_2$Te$_4$.

In this work, we successfully grew single crystals of MnSb$_2$Te$_4$ with Mn-Sb site mixing and reported their structural, magnetic, electronic transport, and thermodynamic properties. Single-crystal x-ray diffraction (XRD) confirmed the presence of Mn-Sb intermixing in the obtained samples, which is consistent with the results reported in Ref. [35]. The magnetic measurements reveal the magnetic anisotropy and ferrimagnetic state of MnSb$_2$Te$_4$, in which the Curie temperature is estimated to be 31 K. Given that our results are distinct from those reported in Ref. [34], the site mixing of Mn and Sb may have a significant influence on the magnetic structure of the MnSb$_2$Te$_4$ samples studied in this work. The largest negative magnetoresistance (MR) of approximately -12% is also found near 30 K. In addition, the Hall resistivity measurement shows an obvious AHE, which may be related to the possible Weyl points driven by the magnetization in this compound.

*chjyi@iphy.ac.cn

II. EXPERIMENT DETAILS

Single crystals of $MnSb_2Te_4$ were synthesized using the flux method. The starting materials Mn (piece, 99.99%), Sb (grain, 99.9999%), and Te (lump, 99.9999%) were mixed in an Ar-filled glove box at a molar ratio of Mn : Sb : Te = 1 : 10 : 16. The mixture was placed in an alumina crucible and sealed in an evacuated quartz tube. The tube was heated to 700 °C for 10 h and dwelt for 20 h. Then, the tube was slowly cooled to 630 °C at a rate of 0.5 °C/h, followed by separation of the crystals from the flux by centrifugation. Large shiny crystals were obtained at the bottom of the crucible.

To investigate the crystalline structure, single-crystal XRD was conducted on a Bruker D8 Venture diffractometer at 273 K using Mo $K\alpha$ radiation ($\lambda = 0.710\,73$ Å). The crystalline structure was refined by the full-matrix least-squares method on F^2 using the SHELXL-2018/3 program. A selected crystal was used for magnetic susceptibility (χ), specific heat (C_p), longitudinal resistivity (ρ), and Hall resistivity (ρ_{xy}) measurements. The magnetic properties were measured in a magnetic properties measurement system (MPMS-III, Quantum Design Inc.) under different applied magnetic fields in field-cooling (FC) and zero-field-cooling (ZFC) modes. Isothermal magnetization (*M-H*) was measured at several fixed temperatures by sweeping the applied field. The transport measurements and the specific heat capacity were measured using a physical property measurement system (Quantum Design Inc.) using a standard DC four-probe technique and a thermal relaxation method, respectively.

III. RESULT AND DISCUSSION

The single-crystal XRD study revealed that $MnSb_2Te_4$ has a structure similar to that of $MnBi_2Te_4$ (space group R-$3m$). The lattice parameters of $MnSb_2Te_4$, $a = 4.2613$ Å and $c = 41.062$ Å, were also close to those of $MnBi_2Te_4$. The presence of Mn-Sb intermixing in $MnSb_2Te_4$ has also been confirmed, which is different from the fully occupied Mn atoms in $MnBi_2Te_4$ but in good accordance with a previous report on polycrystalline samples [35]. As a result, Sb atoms replace approximately 32% of Mn atoms that occupy $3a$ (0.0, 0.0, 0.0)-Mn1, and Mn atoms replace approximately 17.2% of Sb atoms that occupy $6c$ (0.0, 0.0, 0.425 09)-Sb2, respectively. The site mixing causes the ferrimagnetic ground state in $MnSb_2Te_4$, which will be discussed below. The detailed crystallographic data and crystalline parameters obtained from the single-crystal XRD measurements are summarized in Tables I and II. Figure 1(a) shows the XRD patterns of a flat surface of the $MnSb_2Te_4$ single crystal, where only *00l* peaks were detected. A photograph of a typical $MnSb_2Te_4$ crystal is shown in the inset of Fig. 1(a), and a black square of 1 mm × 1 mm indicates the size of the crystal. A schematic drawing of the crystal structure is presented in Fig. 1(b), which shows the mixing of Mn and Sb sites and the alignment of the magnetic moment of the Mn atoms. By drawing the results of the magnetic structure determined in Ref. [35], the large and small arrows roughly represent the magnitude of the magnetic moments for the Mn-rich and Sb-rich layers, respectively.

TABLE I. Crystallographic and structure refinement data for $MnSb_2Te_4$.

Empirical formula	$MnSb_2Te_4$
Formula weight (g mol^{-1})	806.99
Temperature	273(2) K
Wavelength	Mo $K\alpha$ (0.71073 Å)
Crystal system	Trigonal
Space group	R-$3m$ (166)
Unit-cell dimensions (Å)	$a = b = 4.2613(8)$
	$c = 41.062(8)$
Cell volume (Å^3)	645.7(3)
Z	3
Density, calculated (g cm^{-3})	6.226
$h\,k\,l$ range	$-4 \leqslant h \leqslant 5$
	$-5 \leqslant k \leqslant 2$
	$-54 \leqslant l \leqslant 54$
$2\theta_{\min}$ (°)	5.954
$2\theta_{\max}$ (°)	56.308
Linear absorption coeff. (mm^{-1})	20.814
Absorption correction	Multiscan
No. of reflections	2589
$T_{\min}/T_{\max}$	0.3070/0.7457
No. independent reflections	250
No. observed reflections	$229[I > 2\sigma(I)]$
$F(000)$	1003
R indexes	$4.88\%(R_1[F_o > 4\sigma(F_o)])$,
	$15.33\%(wR_2)$
Weighting scheme	$w = 1/[\sigma^2(F_o^2) + (0.0739P)^2,$
	$+29.2319P]$,
	where $P = [\text{Max}(F_o^2) + 2F_c^2]/3$
Refinement software	SHELXL-2018/3

Figure 2 presents the temperature dependences of the magnetic susceptibility measured in applied magnetic fields perpendicular [Figs. 2(a) and 2(b)] and parallel [Figs. 2(c) and 2(d)] to the crystallographic *ab* plane. As shown in Fig. 2(a), an obvious divergence of ZFC and FC susceptibility is observed below approximately 30 K when a 100-Oe magnetic field is applied. The interexchange of Mn atoms at the $3a$ and $6c$ sites causes divergence, suggesting a ferrimagnetic state at low temperatures. The divergence is suppressed to a lower temperature as the applied field increases to 700 Oe and disappears above 1000 Oe. For the magnetic field applied parallel to the *ab* plane [Fig. 2(c)], a similar divergence can be seen in the 100-Oe field. As the applied field increases from 500 to 5000 Oe, the ZFC and FC curves show a sharp

TABLE II. Atomic parameters of $MnSb_2Te_4$.

Atom	Wyckoff	Symmetry	x	y	z	Occup[a]	U_{eq}[b]
Mn1	$3a$	$-3m$	0	0	0	0.680	0.025
Sb1	$3a$	$-3m$	0	0	0	0.320	0.025
Te1	$6c$	$3m$	0	0	0.292 20	1.000	0.024
Mn2	$6c$	$3m$	0	0	0.425 09	0.172	0.028
Sb2	$6c$	$3m$	0	0	0.425 09	0.828	0.028
Te2	$6c$	$3m$	0	0	0.131 36	1.000	0.025

[a]*Occup*: Occupancy.
[b]U_{eq}: equivalent isotropic thermal parameter.
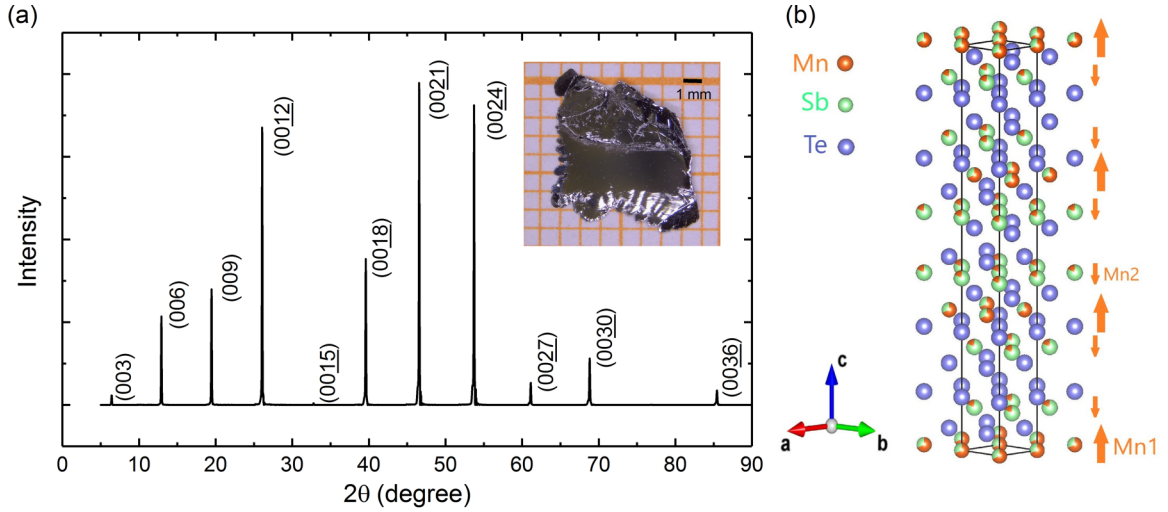
FIG. 1. (a) X-ray diffraction pattern of a flat surface of $MnSb_2Te_4$ single crystal. The inset shows a photograph of a typical $MnSb_2Te_4$ single crystal. (b) The schematic crystalline structure of $MnSb_2Te_4$. The arrows indicate the local magnetic moment of Mn atoms at $3a$ sites and $6c$ sites, respectively.

maximum, which shifts from 30 to 20 K. In addition, the out-of-plane susceptibility is approximately six times larger than the in-plane susceptibility, which indicates that the c axis is the easy magnetization direction. The χ^{-1} vs T curves were fitted by the Curie-Weiss formula of $\chi = C/(T - T_\theta)$, where C is the Curie constant and T_θ is the Weiss temperature. The obtained fitting values for the two field orientations are summarized in Table III for comparison. As shown in Fig. 2(b), the formula of $\chi = C/(T - T_\theta)$ fits the $\chi^{-1} - T$ curve from 250 to 350 K for fields applied perpendicular to the ab plane. The fitting result of $T_\theta = -33$ K is close to the magnetic transition temperature of 31 K obtained from the differential of susceptibility data, indicating a ferrimagnetic phase along the c direction. The effective moment can be roughly defined by $\mu_{\text{eff}} = \sqrt{8C}\mu_B = 7.14\,\mu_B$, which is larger than the theoretical value of $5.92\,\mu_B$ of Mn^{2+} ions in the high-spin state. The effective moment deviates from the theoretical value, which may result from the single-ion anisotropy in $MnSb_2Te_4$. For $H//ab$ in Fig. 2(d), the Curie-Weiss fitting gives a small fitting value of T_θ. The effective moment μ_{eff} was calculated to be approximately $5.56\,\mu_B$. The magnetic anisotropy in $MnSb_2Te_4$ is responsible for the different T_θ and μ_{eff} values for the two field orientations. Previous research by Li *et al.* studied the magnetic anisotropy of the monolayer $MnBi_2Te_4$ based on theoretical calculations and proposed that the magnetic anisotropy originates from single-ion anisotropy induced by the spin-orbit coupling effect of Mn and Te atoms [38]. Single-ion anisotropy enhances the tendency of mo-

ments to align along the easy axis. In $MnSb_2Te_4$, the easy magnetization direction lies along the c axis, which causes anisotropy in the paramagnetic state.

The field dependences of the isothermal magnetization for $H\perp ab$ [Fig. 3(a)] and $H//ab$ [Fig. 3(b)] are different. For $H\perp ab$, the M vs H curve at 5 K shows a small hysteresis loop, indicating a ferrimagnetic order with small coercivity, as shown in Fig. 3(c). The saturated magnetization approaches approximately $2.5\,\mu_B$ at 1 kOe. As the field was applied parallel to the ab plane, the magnetization saturated at a magnetic field of 10 kOe and showed no obvious hysteresis loop. The magnetic measurement results suggest a large anisotropy and indicate that the easy magnetization direction of $MnSb_2Te_4$ lies along the c axis. Owing to the intermixing of Mn and Sb atoms, $MnSb_2Te_4$ exhibits a ferrimagnetic ground state, manifesting a small hysteresis loop, which is different from the antiferromagnetic state of $MnBi_2Te_4$ [28] and $MnSb_2Te_4$ recently reported in Ref. [34]. We have also noticed that the neutron scattering carried by Murakami *et al.* reported the moment of Mn atoms in two sites [35], obtaining the magnetic moment of $4.3\,\mu_B$ for the $3a$ site and $3.1\,\mu_B$ for the $6c$ site. Meanwhile, saturated magnetic moments of our single-crystal sample are in good accordance with the sublattice moment of Mn $2.1\,\mu_B$ per unit cell obtained from neutron scattering.

Figure 4(a) presents the measured specific heat C_P as a function of temperature from 2 to 200 K at zero fields. The blue line is the fitting of C_P using the Debye-Einstein model [39,40]. The analytical formula is as follows:

$$C_{el+ph}(T) = \gamma T + \alpha 9nR\left(\frac{T}{\theta_D}\right)^3 \int_0^{\theta_D/T} \frac{x^4 e^x}{(e^x - 1)^2}dx$$
$$+ (1-\alpha)3nR\frac{\left(\frac{\theta_E}{T}\right)^2 e^{\theta_E/T}}{(e^{\theta_E/T} - 1)^2},$$

where θ_D and θ_E are the Debye and Einstein temperatures, respectively, and α is the contribution ratio of the two components. The fitting parameters were used to simulate the

TABLE III. The fitting values of Curie-Weiss formula for the two field orientations.

Curie-Weiss formula	Field orientations	T_θ (K)	C (emu K/mol)	$\mu_{\text{eff}}(\mu_B)$
$\chi = C/(T - T_\theta)$	$H\perp ab$	-33	6.36	7.14
	$H//ab$	-0.6	4.37	5.56
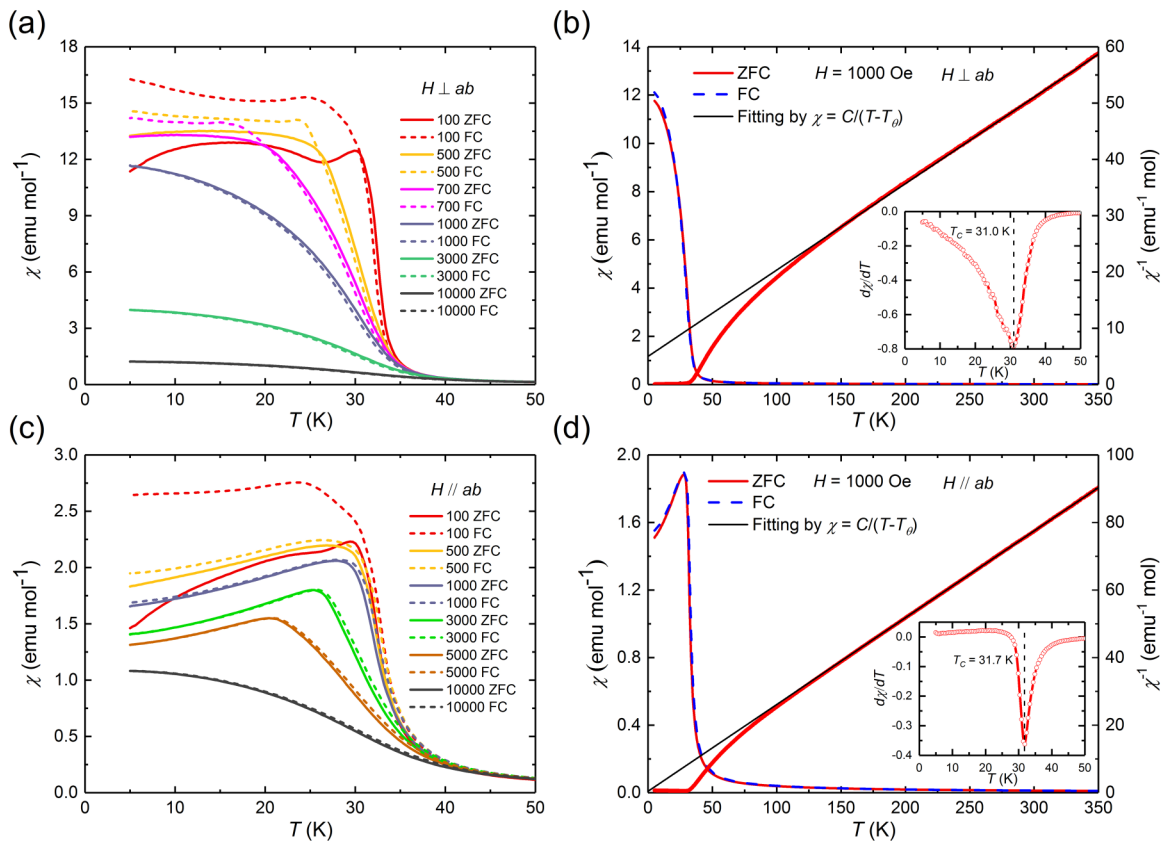
FIG. 2. (a), (c) Temperature dependence of the magnetic susceptibility measured in applied magnetic fields perpendicular and parallel to the crystallographic ab plane. (b), (d) The $\chi-T$ (left) and $\chi^{-1}-T$ (right) curves in the 1000-Oe field; the inset shows the differential of susceptibility below 50 K for defining the Curie temperature.

C_P vs T curve and extend to 2 K and the simulated line, as the background of electron and phonon contributions, enabled us to roughly separate the magnetic contribution from the total C_P. The curve shows a distinct anomaly near 30 K, which is associated with the magnetic transition. The Debye-Einstein model yielded values of $\theta_D = 444$ K, $\theta_E = 110$ K, and $\gamma = 323$ mJ mol^{-1} K^{-2}. The large Sommerfeld coefficient may imply a heavy quasiparticle effective mass in MnSb$_2$Te$_4$. As shown in the inset of Fig. 4(a), we further fitted the specific heat below 20 K using the formula $C_P = \gamma T + \beta T^3 + C_m$, in which the three terms represent electron, phonon, and magnon contributions to the total specific heat,

respectively. For a 3D ferrimagnet system, the magnon contribution part can be expressed as $C_m \sim T^{3/2}\exp(-\Delta/k_BT)$, where Δ is the magnon energy gap. This fitting gives the values of $\gamma = 189$ mJ mol^{-1} K^{-2}, $\beta = 1.4$ mJ mol^{-1} K^{-4}, and $\Delta = 0.88$ meV. We also presented the temperature dependence of the magnetic specific heat C_{mag} in Fig. 4(b), which is calculated by subtracting the fitting data C_{el+ph} from the experimental data C_P. The negative value of C_{mag} below 4 K was caused by the oversubtraction of the total specific heat. The magnetic specific heat blow 10 K is well described by the expression of $C_{mag} \sim T^{d/m}\exp(-\Delta/T)$, yielding $d/m = 1.68$ and $\Delta = 0.92$ meV. This is consistent with the fitting
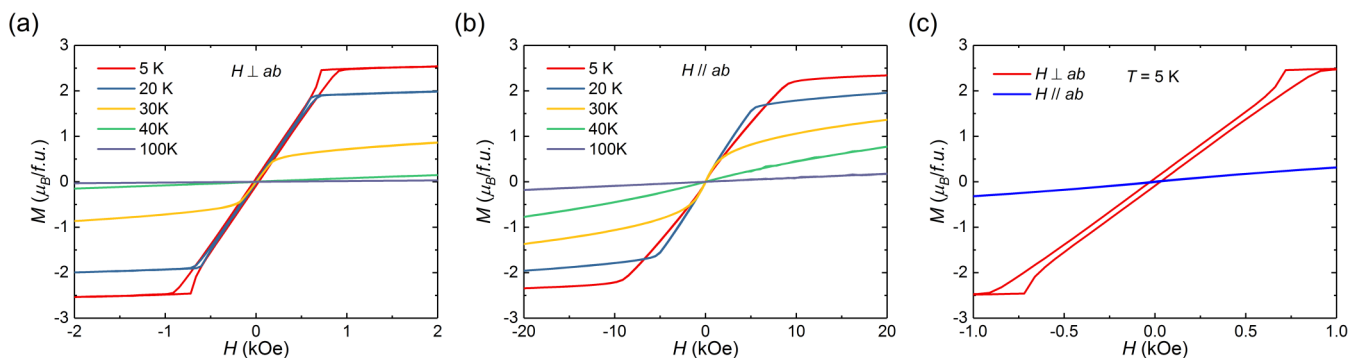
FIG. 3. The field dependence of magnetization at different temperatures for (a) $H\perp ab$ and (b) $H//ab$. (c) The enlarged view of M-H curves at 5 K.
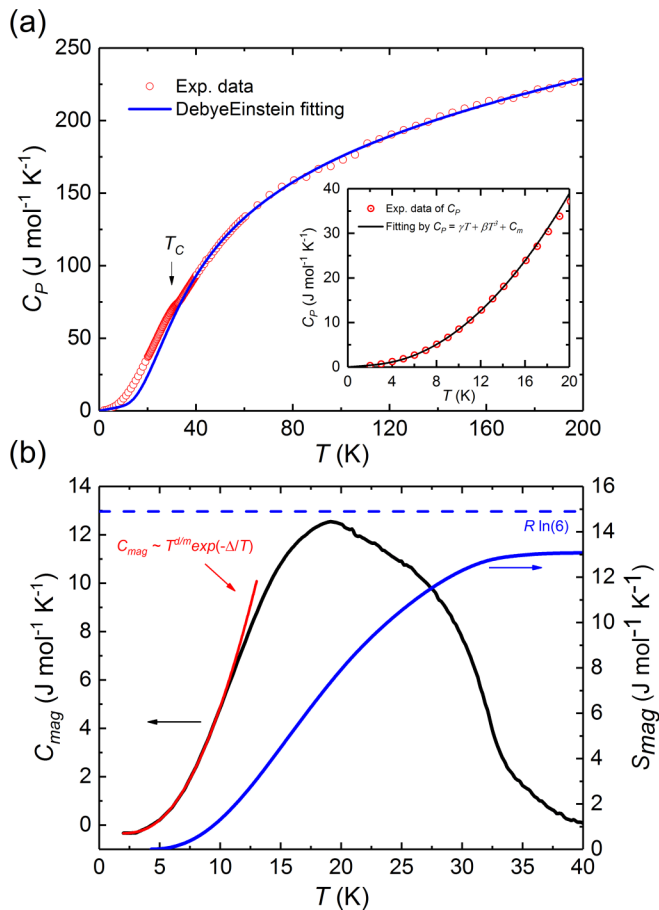
FIG. 4. (a) The measured special heat C_P as a function of temperature and the fitting by Debye-Einstein model. The inset shows C_P vs T curve below 20 K and its fitting. (b) Left: Temperature dependence of the magnetic specific heat C_{mag} and the fitting. Right: The magnetic entropy S_{mag} as a function of temperature below 40 K.

FIG. 5. (a) Temperature dependence of the in-plane electrical resistivity in different applied fields. (b) Field dependence of MR in the magnetic field up to 90 kOe at various temperatures.

results of the C_P data. Figure 4(b) also shows magnetic entropy S_{mag} calculated by the integral of C_{mag}, reaching about 13.1 J mol^{-1} K^{-1} at 40 K, which is slightly smaller than the theoretical value of 14.9 J mol^{-1} K^{-1} for the high-spin state of Mn^{2+} [$S_{mag} = R\ln(2J+1)$ with $J = 5/2$], where R is the gas constant. Additionally, the reduction in S_{mag} may have been caused by the oversubtraction of the total specific heat.

The temperature dependence of the in-plane electrical resistivity ρ_{xx} measured in the temperature range of 5–300 K is presented in Fig. 5(a). Without a magnetic field, the resistivity decreased continually to 70 K, showing a metallic behavior. With further cooling, the resistivity increases, exhibits a cusp around 30 K, and then drops quickly to 2 K. Spin scattering by the intralayer short-range order formed by Mn^{2+} moments could explain the upturn between 30 and 70 K. As the applied field increased, the cusp was suppressed and gradually shifted to higher temperatures. The cusp (or peak) feature of zero-field resistivity near T_C has also been reported in EuB$_6$ [41] EuIn$_2$As$_2$ [42], and EuCd$_2$As$_2$ [43]. In these materials, the spontaneous spin fluctuation above T_C would lead to a large interaction between local moments and charge carriers and form magnetic polarons,

which can localize the conduction carriers. Below T_C, accompanied by the disappearance of spin fluctuation and formation of long-range magnetic order, the magnetic scattering dramatically decreased. When a magnetic field is applied, the cusp is suppressed and shifts toward a high temperature. Figure 5(b) presents the field dependence of the longitudinal magnetoresistance (LMR) in a magnetic field up to 90 kOe at various temperatures. MR was defined as MR(%) $= 100 \times [\rho_{xx}(H) - \rho_{xx}(H = 0)]/\rho_{xx}(H = 0)$. The largest negative LMR reaches 12% at 30 K, which is close to the temperature of the magnetic phase transition. Note that the negative LMR sets at approximately 100 K in MnSb$_2$Te$_4$, which is also a familiar characteristic of magnetic polaron-induced colossal negative magnetoresistance (CMR) systems. This behavior is observed in many magnetic materials such as EuB$_6$ [41,44], Eu$_{14}$MnSb$_{11}$ [45,46], EuIn$_2$As$_2$ [42,47], Eu$_5$In$_2$Sb$_6$ [48], and EuBiTe$_3$ [49], in which the CMR is realized. A common explanation suggests that by applying a magnetic field or lowering the temperature the size of the magnetic polaron can be increased [48,50,51], reducing the hopping energy for conduction carriers, and thus spawning the negative LMR [51]. In MnSb$_2$Te$_4$,

(a)

(b)
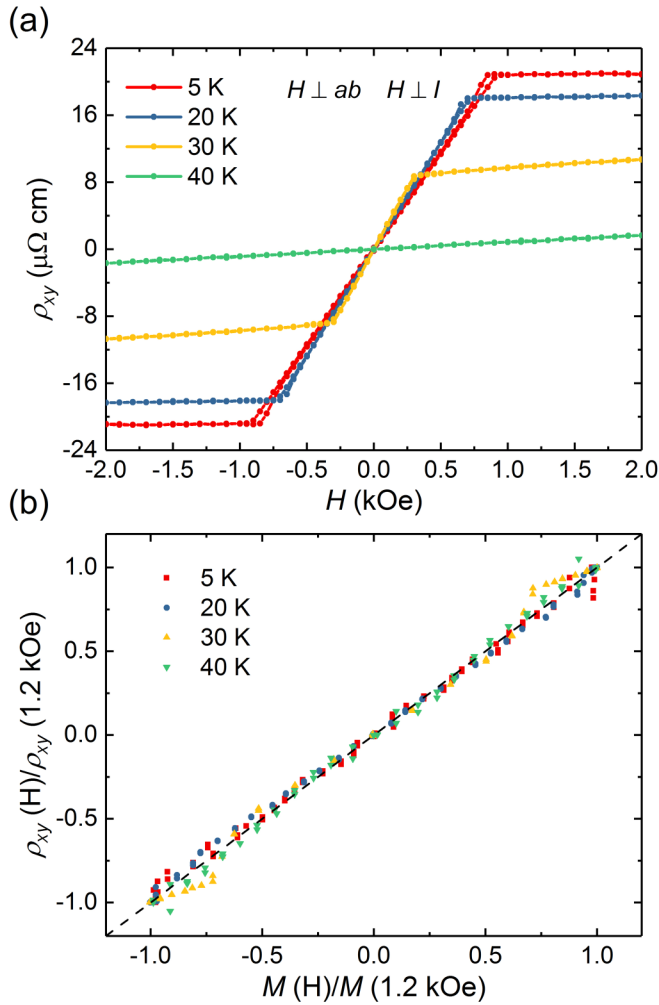
FIG. 6. (a) The field dependence of Hall resistance (ρ_{xy}) at different temperatures. (b) The normalized ρ_{xy} vs normalized M from 5 to 40 K.

although the negative LMR is not as large as the observed CMR in EuB_6 or $Eu_5In_2Sb_6$, it still manifests some features to introduce the interpretation of magnetic polarons. Theoretical calculations have proposed the topological Weyl fermion state in $MnSb_2Te_4$; our results may offer some guidance for further investigation of transport properties that are influenced by both topological nontrivial bands and spin correlations.

Figure 6(a) shows the Hall resistivity ρ_{xy} vs magnetic field H of $MnSb_2Te_4$ in the temperature range of 5–40 K. The $\rho_{xy} - H$ curves exhibit significant temperature dependence, which has a similar trend to that of the field-dependent magnetization curves in Fig. 3(a). At 5 K, ρ_{xy} increases with the application of a magnetic field up to 1 kOe and gradually approaches saturation, indicating that the anomalous Hall resistivity is correlated deeply with magnetization. The Hall resistivity can be described by $\rho_{xy} = R_0 B + \rho_{xy}^A$, where R_0 is the ordinary Hall coefficient and ρ_{xy}^A is the anomalous Hall resistivity [52]. We extracted the ordinary Hall contribution $R_0 B$ from the field-dependent ρ_{xy} at 5 K. The obtained positive $R_0 = 0.067$ cm^3 C^{-1} corresponds to hole-type carriers, and the

estimated carrier density is approximately 9.3×10^{19} cm^{-3}, similar to a previous report in Ref. [34]. For convenience, we plot the normalized ρ_{xy} as a function of the normalized M at different temperatures, as shown in Fig. 6(b). The Hall resistivity and magnetic susceptibility data at all temperatures follow a single straight line, proving that the Hall signal is dominated by the AHE. Notably, compared with the results for bulk samples, the measured AHE on the thin film of $MnSb_2Te_4$ single crystals indicates more obvious hysteresis loops below T_C [36]. We also noticed that the Hall resistivity measured in $MnSb_2Te_4$ samples with antiferromagnetic order, as reported in Ref. [34], is significantly influenced by the spin-flop transition induced by an external magnetic field, which is distinct from our results in this work and on thin films reported in Ref. [36]. The processes of sample growth, including the cooling ratio or annealing time after growth, are responsible for the different atomic coordination of Mn^{2+} ions, yielding different magnetic structures, such as antiferromagnetic [34] or ferrimagnetic alignment. Ferrimagnetic magnetization in $MnSb_2Te_4$ accounts for the AHE because of the residual ferromagnetic component, which is similar to some typical ferromagnetic systems such as Fe/Ni [53,54]. As we did not perform detailed Hall measurements of this compound, it is deceptive to attribute the AHE to the intrinsic contribution from the topological mechanism, for example, the Berry curvature, although $MnSb_2Te_4$ is theoretically predicted to be a topological material.

IV. CONCLUSION

In summary, high-quality single crystals of $MnSb_2Te_4$ grown from Sb-Te flux were systematically studied, including their structural, magnetic, electrical transport, and thermodynamic measurements. A paramagnetic to ferrimagnetic phase transition was observed at $T_C \sim 31$ K. The presence of Mn-Sb intermixing in $MnSb_2Te_4$ was confirmed using single-crystal XRD, which is responsible for the ferrimagnetic ground state instead of the antiferromagnetic state, as reported for $MnSb_2Te_4$ without site mixing and in the analogous $MnBi_2Te_4$. The evolution of the magnetic polaron driven by the temperature and magnetic field dominates the negative LMR at and above T_C. The magnetic structure constructed by Mn^{2+} moments influenced the observed AHE at and below T_C. As a candidate for magnetic Weyl semimetals, the anomalous magnetic and transport phenomena revealed in this work may promote deeper research on the proposed topological properties of this compound.

[1] L. Fu, C. L. Kane, and E. J. Mele, Topological Insulators in Three Dimensions, Phys. Rev. Lett. **98**, 106803 (2007).

[2] L. Fu and C. L. Kane, Topological insulators with inversion symmetry, Phys. Rev. B **76**, 045302 (2007).

[3] M. Z. Hasan and C. L. Kane, Colloquium: Topological insulators, Rev. Mod. Phys. **82**, 3045 (2010).

[4] X.-L. Qi and S.-C. Zhang, Topological insulators and superconductors, Rev. Mod. Phys. **83**, 1057 (2011).

[5] X.-L. Qi, T. L. Hughes, and S.-C. Zhang, Topological field theory of time-reversal invariant insulators, Phys. Rev. B **78**, 195424 (2008).

[6] X.-L. Qi, T. L. Hughes, and S.-C. Zhang, Fractional charge and quantized current in the quantum spin Hall state, Nat. Phys. **4**, 273 (2008).

[7] R. Li, J. Wang, X.-L. Qi, and S.-C. Zhang, Dynamical axion field in topological magnetic insulators, Nat. Phys. **6**, 284 (2010).

[8] N. Varnava and D. Vanderbilt, Surfaces of axion insulators, Phys. Rev. B **98**, 245117 (2018).

[9] C. Yue, Y. Xu, Z. Song, H. Weng, Y.-M. Lu, C. Fang, and X. Dai, Symmetry-enforced chiral hinge states and surface quantum anomalous Hall effect in the magnetic axion insulator $Bi_{2-x}Sm_xSe_3$, Nat. Phys. **15**, 577 (2019).

[10] Y. Xu, Z. Song, Z. Wang, H. Weng, and X. Dai, Higher-Order Topology of the Axion Insulator $EuIn_2As_2$, Phys. Rev. Lett. **122**, 256402 (2019).

[11] F. D. M. Haldane, Model for a Quantum Hall Effect without Landau Levels: Condensed-Matter Realization of the "Parity" Anomaly, Phys. Rev. Lett. **61**, 2015 (1988).

[12] R. Yu, W. Zhang, H.-J. Zhang, S.-C. Zhang, X. Dai, and Z. Fang, Quantized anomalous Hall effect in magnetic topological insulators, Science **329**, 61 (2010).

[13] C.-X. Liu, X.-L. Qi, X. Dai, Z. Fang, and S.-C. Zhang, Quantum Anomalous Hall Effect in $Hg_{1-y}Mn_yTe$ Quantum Wells, Phys. Rev. Lett. **101**, 146802 (2008).

[14] K. Nomura and N. Nagaosa, Surface-Quantized Anomalous Hall Current and the Magnetoelectric Effect in Magnetically Disordered Topological Insulators, Phys. Rev. Lett. **106**, 166802 (2011).

[15] C.-Z. Chang, J. Zhang, X. Feng, J. Shen, Z. Zhang, M. Guo, K. Li, Y. Ou, P. Wei, L.-L. Wang, Z.-Q. Ji, Y. Feng, S. Ji, X. Chen, J. Jia, X. Dai, Z. Fang, S.-C. Zhang, K. He, Y. Wang, L. Lu, X.-C. Ma, and Q.-K. Xue, Experimental observation of the quantum anomalous Hall effect in a magnetic topological insulator, Science **340**, 167 (2013).

[16] J. Wang, B. Lian, and S.-C. Zhang, Quantum anomalous Hall effect in magnetic topological insulators, Phys. Scr. T **164**, 014003 (2015).

[17] R. S. K. Mong, A. M. Essin, and J. E. Moore, Antiferromagnetic topological insulators, Phys. Rev. B **81**, 245209 (2010).

[18] Y. Tokura, K. Yasuda, and A. Tsukazaki, Magnetic topological insulators, Nat. Rev. Phys. **1**, 126 (2019).

[19] L. Šmejkal, Y. Mokrousov, B. Yan, and A. H. MacDonald, Topological antiferromagnetic spintronics, Nat. Phys. **14**, 242 (2018).

[20] P. Tang, Q. Zhou, G. Xu, and S.-C. Zhang, Dirac fermions in an antiferromagnetic semimetal, Nat. Phys. **12**, 1100 (2016).

[21] G. Hua, S. Nie, Z. Song, R. Yu, G. Xu, and K. Yao, Dirac semimetal in type-IV magnetic space groups, Phys. Rev. B **98**, 201116(R) (2018).

[22] L. Šmejkal, J. Železný, J. Sinova, and T. Jungwirth, Electric Control of Dirac Quasiparticles by Spin-Orbit Torque in an Antiferromagnet, Phys. Rev. Lett. **118**, 106402 (2017).

[23] J. Wang, Magnetic Dirac Semimetals in Three Dimensions, arXiv:1701.00896.

[24] X. Wan, A. M. Turner, A. Vishwanath, and S. Y. Savrasov, Topological semimetal and Fermi-arc surface states in the electronic structure of pyrochlore iridates, Phys. Rev. B **83**, 205101 (2011).

[25] G. Xu, H. Weng, Z. Wang, X. Dai, and Z. Fang, Chern Semimetal and the Quantized Anomalous Hall Effect in $HgCr_2Se_4$, Phys. Rev. Lett. **107**, 186806 (2011).

[26] H. Zhang, J. Wang, G. Xu, Y. Xu, and S.-C. Zhang, Topological States in Ferromagnetic CdO/EuO Superlattices and Quantum Wells, Phys. Rev. Lett. **112**, 096804 (2014).

[27] M. M. Otrokov, I. I. Klimovskikh, H. Bentmann, A. Zeugner, Z. S. Aliev, S. Gass, A. U. B. Wolter, A. V. Koroleva, D. Estyunin, A. M. Shikin, M. Blanco-Rey, M. Hoffmann, A. Y. Vyazovskaya, S. V. Eremeev, Y. M. Koroteev, I. R. Amiraslanov, M. B. Babanly, N. T. Mamedov, N. A. Abdullayev, V. N. Zverev, B. Büchner, E. F. Schwier, S. Kumar, A. Kimura, L. Petaccia, G. Di Santo, R. C. Vidal, S. Schatz, K. Kißner, C.-H. Min, S. K. Moser, T. R. F. Peixoto, F. Reinert, A. Ernst, P. M. Echenique, A. Isaeva, and E. V. Chulkov, Prediction and observation of the first antiferromagnetic topological insulator, Nature (London) **576**, 416 (2019).

[28] D. Zhang, M. Shi, T. Zhu, D. Xing, H. Zhang, and J. Wang, Topological Axion States in the Magnetic Insulator $MnBi_2Te_4$ with the Quantized Magnetoelectric Effect, Phys. Rev. Lett. **122**, 206401 (2019).

[29] J. Li, Y. Li, S. Du, Z. Wang, B.-L. Gu, S.-C. Zhang, K. He, W. Duan, and Y. Xu, Intrinsic magnetic topological insulators in van der Waals layered $MnBi_2Te_4$-family materials, Sci. Adv. **5**, eaaw5685 (2019).

[30] Y. Gong, J. Guo, J. Li, K. Zhu, M. Liao, X. Liu, Q. Zhang, L. Gu, L. Tang, X. Feng, D. Zhang, W. Li, C. Song, L. Wang, P. Yu, X. Chen, Y. Wang, H. Yao, W. Duan, Y. Xu, S.-C. Zhang, X. Ma, Q.-K. Xue, and K. He, Experimental realization of an intrinsic magnetic topological insulator, Chin. Phys. Lett. **36**, 076801 (2019).

[31] R. C. Vidal, H. Bentmann, T. R. F. Peixoto, A. Zeugner, S. Moser, C.-H. Min, S. Schatz, K. Kißner, M. Ünzelmann, C. I. Fornari, H. B. Vasili, M. Valvidares, K. Sakamoto, D. Mondal, J. Fujii, I. Vobornik, S. Jung, C. Cacho, T. K. Kim, R. J. Koch, C. Jozwiak, A. Bostwick, J. D. Denlinger, E. Rotenberg, J. Buck, M. Hoesch, F. Diekmann, S. Rohlf, M. Kalläne, K. Rossnagel, M. M. Otrokov, E. V. Chulkov, M. Ruck, A. Isaeva, and F. Reinert, Surface states and Rashba-type spin polarization in antiferromagnetic $MnBi_2Te_4$ (0001), Phys. Rev. B **100**, 121104(R) (2019).

[32] Y. Deng, Y. Yu, M. Z. Shi, Z. Guo, Z. Xu, J. Wang, X. H. Chen, and Y. Zhang, Quantum anomalous Hall effect in intrinsic magnetic topological insulator $MnBi_2Te_4$, Science **367**, 895 (2020).

[33] J. Ge, Y. Liu, J. Li, H. Li, T. Luo, Y. Wu, Y. Xu, and J. Wang, High-Chern-number and high-temperature quantum Hall effect without Landau levels, Natl. Sci. Rev. **7**, 1280 (2020).

[34] J.-Q. Yan, S. Okamoto, M. A. McGuire, A. F. May, R. J. McQueeney, and B. C. Sales, Evolution of structural, magnetic, and transport properties in MnBi$_{2-x}$Sb$_x$Te$_4$, Phys. Rev. B **100**, 104409 (2019).

[35] T. Murakami, Y. Nambu, T. Koretsune, G. Xiangyu, T. Yamamoto, C. M. Brown, and H. Kageyama, Realization of interlayer ferromagnetic interaction in MnSb$_2$Te$_4$ toward the magnetic Weyl semimetal state, Phys. Rev. B **100**, 195103 (2019).

[36] G. Shi, M. Zhang, D. Yan, H. Feng, M. Yang, Y. Shi, and Y. Li, Anomalous Hall effect in layered ferrimagnet MnSb$_2$Te$_4$, Chin. Phys. Lett. **37**, 047301 (2020).

[37] L. Zhou, Z. Tan, D. Yan, Z. Fang, Y. Shi, and H. Weng, Topological phase transition in the layered magnetic compound MnSb$_2$Te$_4$: Spin-orbit coupling and interlayer coupling dependence, Phys. Rev. B **102**, 085114 (2020).

[38] Y. Li, Z. Jiang, J. Li, S. Xu, and W. Duan, Magnetic anisotropy of the two-dimensional ferromagnetic insulator MnBi$_2$Te$_4$, Phys. Rev. B **100**, 134438 (2019).

[39] S. Baran, D. Kaczorowski, A. Arulraj, B. Penc, and A. Szytuła, Magnetic structure and thermodynamic properties of TmPtIn, J. Magn. Magn. Mater. **322**, 2177 (2010).

[40] C. L. Yang, X. Wang, X. Zhang, D. S. Wu, M. Liu, P. Zheng, J. Y. Yao, Z. Z. Li, Y.-F. Yang, Y. G. Shi, J. L. Luo, and N. L. Wang, Kondo effect in the quasiskutterudite Yb$_3$Os$_4$Ge$_{13}$, Phys. Rev. B **91**, 075120 (2015).

[41] S. Süllow, I. Prasad, M. C. Aronson, S. Bogdanovich, J. L. Sarrao, and Z. Fisk, Metallization and magnetic order in EuB$_6$, Phys. Rev. B **62**, 11626 (2000).

[42] A. M. Goforth, P. Klavins, J. C. Fettinger, and S. M. Kauzlarich, Magnetic properties and negative colossal magnetoresistance of the rare earth Zintl phase EuIn$_2$As$_2$, Inorg. Chem. **47**, 11048 (2008).

[43] M. C. Rahn, J.-R. Soh, S. Francoual, L. S. I. Veiga, J. Strempfer, J. Mardegan, D. Y. Yan, Y. F. Guo, Y. G. Shi, and A. T. Boothroyd, Coupling of magnetic order and charge transport in the candidate Dirac semimetal EuCd$_2$As$_2$, Phys. Rev. B **97**, 214422 (2018).

[44] C. N. Guy, S. von Molnar, J. Etourneau, and Z. Fisk, Charge transport and pressure dependence of T_C of single crystal, ferromagnetic EuB$_6$, Solid State Commun. **33**, 1055 (1980).

[45] J. Y. Chan, S. M. Kauzlarich, P. Klavins, R. N. Shelton, and D. J. Webb, Colossal magnetoresistance in the transition-metal Zintl compound Eu$_{14}$MnSb$_{11}$, Chem. Mater. **9**, 3132 (1997).

[46] J. Y. Chan, S. M. Kauzlarich, P. Klavins, R. N. Shelton, and D. J. Webb, Colossal negative magnetoresistance in an antiferro-magnet, Phys. Rev. B **57**, R8103 (1998).

[47] Y. Zhang, K. Deng, X. Zhang, M. Wang, Y. Wang, C. Liu, J.-W. Mei, S. Kumar, E. F. Schwier, K. Shimada, C. Chen, and B. Shen, In-plane antiferromagnetic moments and magnetic polaron in the axion topological insulator candidate EuIn$_2$As$_2$, Phys. Rev. B **101**, 205126 (2020).

[48] P. Rosa, Y. Xu, M. Rahn, J. Souza, S. Kushwaha, L. Veiga, A. Bombardi, S. Thomas, M. Janoschek, E. Bauer, M. Chan, Z. Wang, J. Thompson, N. Harrison, P. Pagliuso, A. Bernevig, and F. Ronning, Colossal magnetoresistance in a nonsymmorphic antiferromagnetic insulator, Npj Quantum Mater. **5**, 52 (2020).

[49] Y. Y. Niu, D. Wu, L. Shen, and B. Wang, A layered antiferromagnetic semiconductor EuMTe$_3$ (M = Bi, Sb), Phys. Status Solidi RRL **9**, 735 (2015).

[50] A. Amyan, P. Das, J. Müller, and Z. Fisk, Electronic phase separation due to magnetic polaron formation in the semimetallic ferromagnet EuB$_6$ — a weakly-nonlinear-transport Study, J. Korean Phys. Soc. **62**, 1489 (2013).

[51] W. Shon, J.-S. Rhyee, Y. Jin, and S.-J. Kim, Magnetic polaron and unconventional magnetotransport properties of the single-crystalline compound EuBiTe$_3$, Phys. Rev. B **100**, 024433 (2019).

[52] N. Nagaosa, J. Sinova, S. Onoda, A. H. MacDonald, and N. P. Ong, Anomalous Hall effect, Rev. Mod. Phys. **82**, 1539 (2010).

[53] Y. Tian, L. Ye, and X. Jin, Proper Scaling of the Anomalous Hall Effect, Phys. Rev. Lett. **103**, 087206 (2009).

[54] E. M. Pugh and N. Rostoker, Hall effect in ferromagnetic materials, Rev. Mod. Phys. **25**, 151 (1953).